Accepted Manuscript

Simultaneously achieving large ferroelectric polarization and high-T_C in sol-gel deposited PbTiO$_3$-based perovskite thin films

Mengqi Ye[a,b,#], Jin Liu[a,#], Duo Wang[c,#], Zhao Pan[a,*], Fengyi Zhou[c], Xubin Ye[a], Huajie Luo[d], Nianpeng Lu[a], Yunzhong Chen[a], Ruilong Wang[b], and Youwen Long[a,e,*]

[a]Beijing National Laboratory for Condensed Matter Physics, Institute of Physics, Chinese Academy of Sciences, Beijing 100190, China

[b]Key Laboratory for Intelligent Sensing System and Security of Ministry of Education, School of Physics & School of Microelectrics, Hubei University, Wuhan 430062, People's Republic of China

[c]Faculty of Applied Sciences, Macao Polytechnic University, Macao, SAR, China

[d]School of Materials Science and Engineering, University of Science and Technology Beijing, Beijing 100083 China

[e]Songshan Lake Materials Laboratory, Dongguan, Guangdong 523808, China

[#]These authors contributed equally to this work.

Corresponding author: zhaopan@iphy.ac.cn and ywlong@iphy.ac.cn

Physical Chemistry Chemical Physics Accepted Manuscript

Abstract

Perovskite-type thin films based on BiMeO$_3$-PbTiO$_3$ have been intensively studied due to their promising applications in ferroelectric and electronic devices. Nevertheless, achieving high Curie temperature (T_C) while maintaining robust ferroelectric polarization in BiMeO$_3$-PbTiO$_3$ thin films remains a significant challenge. In this study, we deposited 0.1Bi(Zn$_{2/3}$Nb$_{1/3}$)O$_3$-0.9PbTiO$_3$ perovskite thin films onto Pt(111)/Ti/SiO$_2$/Si substrates using the traditional sol-gel method. Through the incorporation of a PbO seeding layer, the thin films manifested excellent crystallization characteristics, featuring a phase-pure perovskite structure accompanied by a uniform and dense microstructure. Consequently, the films demonstrate large ferroelectric remanent polarization (P_r) values of 2P_r ~ 174 and 118 μC cm^{-2} under normal mode and PUND mode measurements, respectively, highlighting the P_r values reported in BiMeO$_3$-PbTiO$_3$ thin films to date. Furthermore, the thin films exhibit a high T_C of 468 °C. First-principles calculations revealed that the strong hybridizations of Pb/Bi-O and Ti/Zn/Nb-O bonds are responsible for the large ferroelectric polarization. The comprehensive high-performance ferroelectric properties of the present 0.1Bi(Zn$_{2/3}$Nb$_{1/3}$)O$_3$-0.9PbTiO$_3$ thin films highlight their potential for FeRAM applications.

Introduction

Ferroelectric materials, particularly perovskite-type (ABO_3) thin films, have garnered significant attention in the development of advanced technologies such as microelectromechanical systems (MEMS) and nonvolatile ferroelectric random access memories (FeRAM),[1–4] because of their excellent ferroelectric properties. However, a high Curie temperature (T_C) is essential for ensuring reliable performance in demanding environments, particularly in industries such as automotive, aerospace, and power generation. Therefore, exploring ferroelectric materials with elevated T_C is imperative to meet the evolving demands of modern technology. Moreover, their high ferroelectric performance can improve the reliability of memory devices, enable sensors to achieve higher signal output, and enhance the practicality of the devices.

$PbTiO_3$ is a typical tetragonal perovskite ferroelectric material, renowned for its large spontaneous polarization ($P_S = 68\ \mu C\ cm^{-2}$) and high Curie temperature ($T_C = 490$ °C).[5,6] Notably, the tetragonal structure of $PbTiO_3$ can be effectively stabilized over a wide range through chemical modifications. In 2002, the xBiScO$_3$-(1-x)PbTiO$_3$ solid solutions were reported to exhibit excellent piezoelectric properties and high T_C near the morphotropic phase boundary.[7–10] This discovery sparked significant interests in BiMeO$_3$-PbTiO$_3$ solid solutions, where Me can be a single trivalent cation or a combination of cations with an average valence of +3.[7,11,12] In these perovskites, strong hybridizations between the A-site Bi^{3+}/Pb^{2+} ions, which possess unique $6s^2$ lone-pair electrons, and oxygen contribute to their robust ferroelectricity.[13] Furthermore, the B-site ions, such as Ti, Fe, and Zn, which are ferroelectric-active cations, can also form

strong hybridizations with oxygen, further enhancing the ferroelectric polarization and T_C.[14] The versatility of BiMeO$_3$-PbTiO$_3$ solid solutions stems from the wide variety of B-site cations available. However, the metastable nature of most BiMeO$_3$ end members often results in limited solubility between PbTiO$_3$ and BiMeO$_3$ compounds, typically requiring high-pressure synthesis methods to produce high-purity BiMeO$_3$-PbTiO$_3$ compounds.[15,16] Thin films, which can induce internal stress through substrate interactions, offer an effective and alternative approach to stabilizing the metastable structure of the BiMeO$_3$-PbTiO$_3$.[17] Indeed, high-performance ferroelectric properties have been reported in various BiMeO$_3$-PbTiO$_3$ thin films, such as Bi(Cu$_{1/2}$Ti$_{1/2}$)O$_3$-PbTiO$_3$, Bi(Zn$_{1/2}$Zr$_{1/2}$)O$_3$-PbTiO$_3$, and Bi(Ni$_{1/2}$Hf$_{1/2}$)O$_3$-PbTiO$_3$.**Error! Reference source not found.**[–19] Notably, most BiMeO$_3$-PbTiO$_3$ thin films usually exhibit larger remanent polarization (P_r) values compared with Hf-based fluorite ferroelectrics,[20,21] and some systems even show comparable P_r and T_C to that of the well-known AlScN-based wurtzite ferroelectrics.[22,23] However, to date, few BiMeO$_3$-PbTiO$_3$ thin films have simultaneously achieved large ferroelectric polarization and high-T_C. Achieving a high T_C while maintaining robust ferroelectric polarization in BiMeO$_3$-PbTiO$_3$ thin films remains a significant challenge.

Previous studies have demonstrated that Bi(Zn$_{1/2}$Ti$_{1/2}$)O$_3$ and Bi(Zn$_{1/2}$V$_{1/2}$)O$_3$ perovskite compounds exhibit strong polarity, suggesting that Zn^{2+} can enhance ferroelectric properties.[15,24] Additionally, the addition of Nb^{5+} in traditional PZT has been reported to dramatically increase its T_C from 386 °C to 443 °C.[25,26] Based on these findings, we report the preparation of 0.1Bi(Zn$_{2/3}$Nb$_{1/3}$)O$_3$-0.9PbTiO$_3$ (0.1BZN-0.9PT)

thin films using a traditional sol-gel deposition method. As expected, the resulting

0.1BZN-0.9PT thin films exhibit both large ferroelectric spontaneous polarization and

a high-T_C. A systematic investigation of crystal structure and ferroelectric properties

was conducted.

Experimental methods

The 0.1BZN-0.9PT thin films were fabricated on the Pt(111)/Ti/SiO$_2$/Si substrates

via a typical sol-gel deposition method. The raw materials are lead acetate trihydrate

[Pb(COOCH$_3$)$_2$·3H$_2$O], titanium n-butoxide [Ti(OC$_4$H$_9$)$_4$], bismuth nitrate

pentahydrate [Bi(NO$_3$)$_3$·5H$_2$O], Nb(OC$_2$H$_5$)$_5$ and Zn(CH$_3$COO)$_2$. The 2-

methoxyethanol, deionized water and glacial acetic acid were used as solvent, chelator

and stabilizer, respectively. Additionally, 10 mol% Pb and 6 mol% Bi were introduced

into the precursor solution to compensate for the loss of Pb and Bi elements during the

sample preparation. Then, the BZN-PT precursor solution (0.2 M) was obtained with

stirring at room temperature.

We spin-coated single PbO layer as a seed layer to improve the crystallinity of the

BZN-PT thin films.[27–29] First of all, the PbO seed layer was spin-coated on

Pt(111)/Ti/SiO$_2$/Si substrate, then the wet film was pyrolyzed for 10 min. Next, the

precursor solution was spin-coated above PbO seed layer. Note that the spin-coated and

pyrolysis processes repeated several times to reach a thickness of about 280 nm. Finally,

the thin films were annealed at 700 °C for 45min.

The microstructure was analyzed by X-ray diffraction (XRD, D2 Phaser, Bruker,

Germany and Rigaku, D/max-2000, Cu Kα radiation). Transmission electron

microscopy (TEM), selected area electron diffraction (SAED), and the high-angle annular dark field (HAADF) investigations were performed by transmission electron microscope (JEM-ARM200F, JEOL, Japan). The FIB sampling was performed using a Focused Ion Beam Scanning electron Microscopy (FIB/SEM, Crossbeam 550, ZEISS, Germany). The cross-sectional morphology of the films was examined by the field emission scanning electron microscope (FE-SEM, SU8220, Hitachi, Japan). The morphology of the as-deposited thin films was characterized using an atomic force microscope (AFM, MultiMode 8, Bruker, Germany). Ferroelectric property measurement and leakage current were carried out with ferroelectric analyzer (TF-Analyzer 3000, aix ACCT, Germany). Dielectric properties were tested by using impedance analyzer (Impedance Analyzer E4990A, KEYSIGHT, America).

The structural model was built based on the experimentally measured crystal structure, with $P4mm$ space group and lattice parameters of 3.91, 3.91, and 4.18 Å, respectively. To satisfy the compositional ratio requirement and maintain high computational efficiency, a $2 \times 5 \times 3$ supercell, with the lattice parameters of 7.81, 19.54 and 12.54 Å was employed to represent the 10 % doping effect in $0.1Bi(Zn_{2/3}Nb_{1/3})O_3$-$0.9PbTiO_3$. The model has a total of 150 atoms, including 27 Pb, 27 Ti, 3 Bi, 2 Zn, 1 Nb, and 90 O atoms. The 3 Bi atoms and 2 Zn/1 Nb atoms are randomly substituted at the corresponding A and B sites, respectively, to simulate the atomic environment of the experimental solid solution. Our simulations are based on the first-principles electronic structure calculations within density functional theory (DFT), and are performed by the Vienna ab initio simulation package (VASP) that

Physical Chemistry Chemical Physics

employs a plane wave basis set.[30] The generalized gradient approximation with Perdew-Burke-Ernzerhof functional[31] is used for describing electron exchange-correlation interactions.[32] A 500 eV cutoff energy is adopted for the appropriate plane wave region. In the geometry optimization, the volume and cell shape are fixed, and the internal atomic positions are fully relaxed. The convergence criteria for energy and force are set to 1×10^{-6} eV and 0.01 eV/Å, respectively. Meanwhile, a Monkhorst-Pack mesh of $5 \times 2 \times 3$ k-points and $7 \times 3 \times 4$ k-points are used for the structure optimization and the investigation of the electron localization function[33] and Bader charge[34] for obtaining the bonding information, respectively.

Results and discussion

The XRD patterns of the pristine PT and 0.1BZN-0.9PT thin films are shown in Fig. 1. As can be seen, pristine PT exhibits a tetragonal symmetry, while the 0.1BZN-0.9PT thin films appear to exhibit a pseudo-cubic perovskite structure. Notably, to enhance crystallinity and control facet orientation, a PbO seed layer was spin-coated onto the Pt(111)/Ti/SiO$_2$/Si substrate prior to the deposition of the 0.1BZN-0.9PT thin films. To confirm the presence of the PbO seeding layer, the HAADF imaging was conducted on two selected regions of the 0.1BZN-0.9PT thin films (Fig. S1a and Fig. S1c). Fig. S1a presents a HAADF image of the region between the substrate and the 0.1BZN-0.9PT thin films, while Fig. S1b displays the corresponding Fourier transform (FFT) results. Based on these findings, we calculated the interplanar spacing (d) values

for specific planes (*hkl*), which are consistent with the structure of PbO. The crystal

structure of PbO is tetragonal with the space group of *P*4/nmm. Additionally, a HAADF

image of the region away from the substrate is also investigated (Fig. S1c). The FFT

results indicate the tetragonal nature of the 0.1BZN-0.9PT thin films (Fig. S1d).

Additionally, an apparent asymmetry can be observed for the (100) diffraction peak.

We therefore performed peak-fitting on the diffraction peak near 22.5° of the 0.1BZN-

0.9PT thin films (see the inset of Fig. 1). The peak can be well-fitted by two components

corresponding to the (001) and (100) planes, respectively, indicating a tetragonal

structure similar to that of pristine PT. The tetragonal nature of the 0.1BZN-0.9PT thin

films can be further confirmed by the HAADF experiments mentioned above. It is

worth noting that the 0.1BZN-0.9PT thin films exhibit a smaller *c*/*a* ratio compared to

PT, which is usually observed in $PbTiO_3$-based perovskites.[35−37] The reduction in the

c/*a* ratio can be attributed to internal stresses within the BZN-PT films, arising from the

mismatch in thermal expansion coefficients between the BZN-PT films and the

substrate. The decrease in the *c*/*a* ratio is accompanied by a corresponding reduction in

domain-wall energy, which can facilitate domain switching during the poling process.
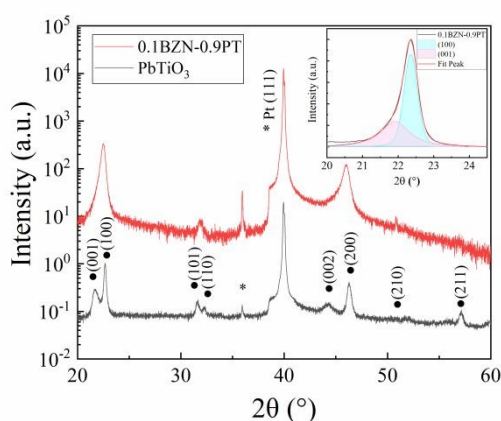
Fig. 1. XRD patterns of $PbTiO_3$ and 0.1BZN-0.9PT thin films. The inset shows the peak fitting of

the 0.1BZN-0.9PT thin films in the range of 20°−24°.
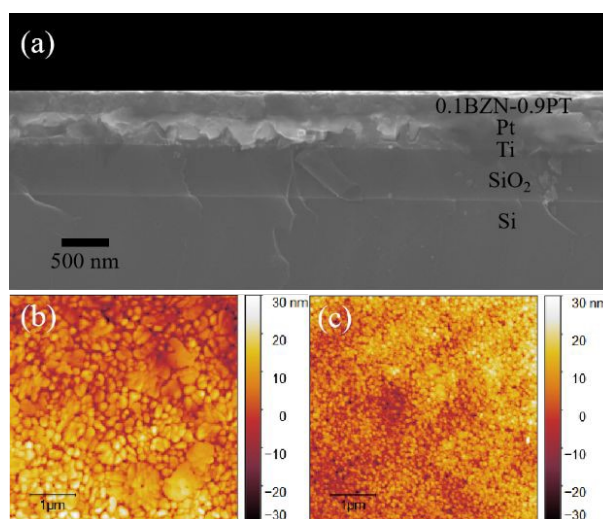
Fig. 2. (a) Cross-sectional SEM image of the 0.1BZN-0.9PT thin films, AFM images of (b)

$PbTiO_3$ and (c) 0.1BZN-0.9PT thin films, respectively.

Fig. 2a presents the cross-sectional SEM micrograph of the BZN-PT thin films,

which reveals a clear interface between the films and the substrate. The thin films

exhibit a dense and uniform microstructure with a smooth surface, having a thickness

of approximately 280 nm. Figs. 2b and 2c display the surface morphologies of the

$PbTiO_3$ and 0.1BZN-0.9PT thin films, respectively, as measured by AFM. The AFM

images indicate that the grain size of $PbTiO_3$ thin films is ranging from 100 to 300 nm, while the 0.1BZN-0.9PT thin films exhibit smaller and more uniform grains, approximately 50-100 nm. The reduction in grain size can be attributed to the introduction of Zn/Nb ions, which are commonly used as sintering aids in ceramics.[38],[39] Furthermore, the 0.1BZN-0.9PT thin films also show a smoother surface, with an RMS roughness of 6.793 nm, compared to that of the $PbTiO_3$ thin films (7.499 nm). Generally, a uniform microstructure in thin films is beneficial for the poling process during ferroelectric measurements.[35−37]
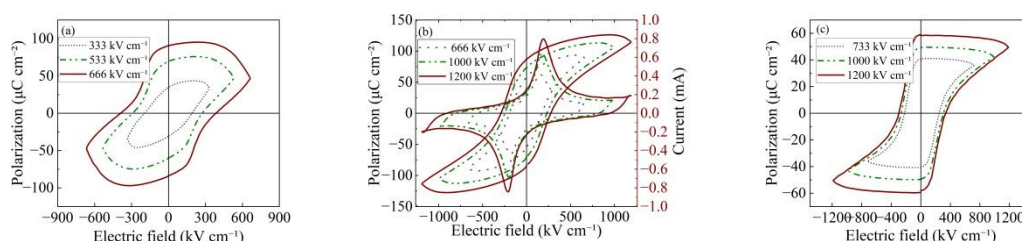
Fig. 3. (a) Ferroelectric hysteresis *P-E* loops for the PT thin films, (b) Ferroelectric hysteresis *P-E* loops and switching currents for the 0.1BZN-0.9PT thin films, (c) Ferroelectric hysteresis *P-E* loops for the 0.1BZN-0.9PT thin films at the PUND mode.

To investigate the ferroelectric properties of the pure PT and 0.1BZN-0.9PT thin films, we conducted typical ferroelectric polarization versus electric field (*P-E*) loop measurements under different electric fields, as shown in Fig. 3. The *P-E* loops of PT are rounded and broad even at low electric fields (Fig. 3a), suggesting the strong leakage current of pure PT thin films. In contrast, the 0.1BZN-0.9PT film exhibits slender *P-E* loops, indicating the high-quality of the thin films. Moreover, the 0.1BZN-0.9PT thin films exhibit a trend toward saturation as the electric field increases (Fig. 3b). However, applying an electric field exceeding 1200 kV cm^{-1} leads to significant

leakage current and potential film breakdown. Therefore, we measured the P-E loops at the maximum electric field that the films can withstand. As shown in Fig. 3b, the 0.1BZN-0.9PT thin films demonstrate a large remanent polarization (P_r) value of $2P_r \sim$ 174 μC cm^{-2}, and a coercive field (E_C) of approximately 275 kV cm^{-1}. The two peaks in the current versus electric field curves are due to the polarization-switching current. It is proposed that typical P-E loops consist of three primary contributions: switching current, dielectric displacement current, and leakage current.[40,41] The dielectric current corresponds to the capacitive component of the signal, while the leakage current arises from oxide vacancies and other defect movements within the film.[40] To further understand the leakage behavior, we measured the leakage current of the thin films, as presented in Fig. S3. The introduction of BZN significantly reduced the leakage current from 8.7×10^{-3} A cm^{-2} of pure PT thin films, to 2.7×10^{-6} A cm^{-2} for the 0.1BZN-0.9PT thin films. Here the leakage current of pristine PT thin films is comparable to previous study.[42] To obtain the intrinsic ferroelectric polarization, we employed the positive-up negative-down (PUND) pulse method[43] to measure the P-E loops of 0.1BZN-0.9PT thin films (Fig. 3c). The PUND method effectively minimizes the contributions of dielectric current and leakage current, allowing us to isolate the intrinsic remanent polarization.**Error! Reference source not found.** From the PUND measurements, a large $2P_r$ value of approximately 118 μC cm^{-2} was observed, with an E_C of about 336 kV cm^{-1}. For comparison, the P_r value reported here is much higher than most BiMeO$_3$-PbTiO$_3$ thin films (Table S1). However, the P_r of 0.1BZN-0.9PT thin films is still lower than the Al$_{0.8}$Sc$_{0.2}$N thin films, which show a large P_r of approximately 135 μC cm^{-2} prepared

by dual-source radio frequency reaction magnetron sputtering.[44−46] Note that the relatively high E_C observed in this study can be attributed to the small grain size and the large c/a ratio. Generally, the c/a ratio significantly influences domain switching behavior.[44,47] A higher c/a value corresponds to greater lattice distortion, which suppresses the nucleation of new domains due to increased elastic energy within the domain walls.[48] Consequently, a high E_C is typically accompanied by a large c/a ratio.[47] The robust ferroelectric polarization of the present 0.1BZN-0.9PT thin films can be attributed to their relatively large c/a ratio and uniform microstructure. The large c/a ratio is closely associated with the large P_S displacement, which is the fundamental origin of ferroelectric polarization.[49,50]
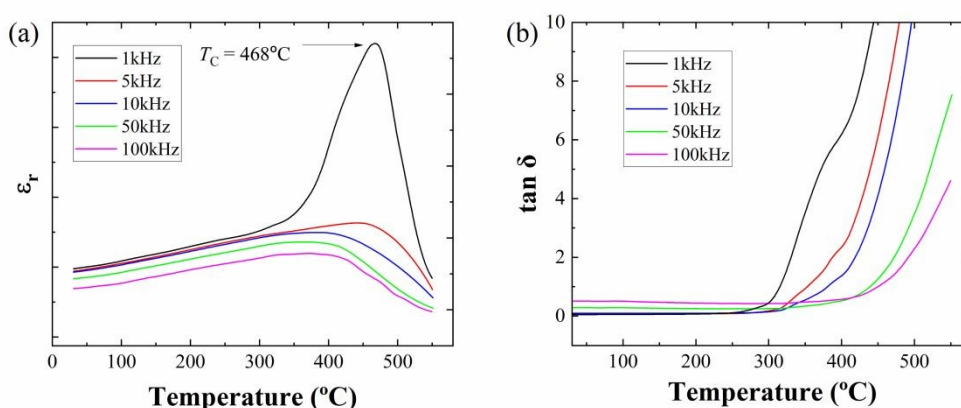
Fig. 4. Temperature dependent the dielectric constant and dielectric loss of the BZN-PT thin films.

Since the 0.1BZN-0.9PT thin films exhibit large ferroelectric polarization, the T_C is another critical parameter for high-performance ferroelectric materials. To determine the T_C, we measured the dielectric permittivity (ε_r) as a function of temperature at different frequencies, as shown in Fig. 4. The dielectric peak of the 0.1BZN-0.9PT thin films occurs at approximately 468 °C, corresponding to the ferroelectric-to-paraelectric

phase transition, that is, the T_C.[51] It is important to note that the phase transition occurs

over a wide temperature range at higher frequencies. The ε_r value should be interpreted

with caution, as they may be easily affected by probe vibration caused by thermal

expansion during the measurements. Therefore, we didn't show the dielectric

permittivity. However, the phase transition temperature should be reliable, since it only

depends on temperature. To further confirm the T_C, we also conducted temperature-

dependent XRD experiments on the 0.1BZN-0.9PT thin films, as shown in Fig. S2a.

Additionally, to investigate the phase transition and accurately determine the T_C, we

performed a detailed analysis of the (100) diffraction peak by peak fitting, as presented

in Fig. S2b. At low temperatures, the peak around 22.5° exhibits asymmetry and can be

well fitted by two peaks corresponding to the (001) and (100) planes, indicating a

tetragonal structure. However, as the temperature approaches the T_C, the peak gradually

becomes symmetric. The detailed lattice constants as a function of temperature are

presented in Fig. S2c. It can be seen that the phase transition temperature (T_C) is

approximately 500 °C. Note that the T_C determined by dielectric measurements is

lower than that determined by temperature-dependent XRD data. One possible reason

for this discrepancy may be the different accuracy of sample temperatures during

dielectric and temperature-dependent XRD measurements. Additionally, XRD

measurements usually require a certain degree of lattice distortion to detect structural

changes, and a clear signal can only be observed when the phase transition is

completed.[52] Therefore, the measured T_C is more representative of the end temperature

of the phase transition. In contrast, dielectric measurements are particularly sensitive to

local polarization changes. Even if the structure has not fully transformed, as long as there is a significant anomaly in the polarization response, the T_C can be detected.[53,54] Therefore, the T_C measured by the dielectric constant method is likely to be slightly lower than that measured by temperature-dependent XRD experiments. Thus, the T_C of the thin film is about 468 ℃, suggesting its potential to work under high-temperature conditions.
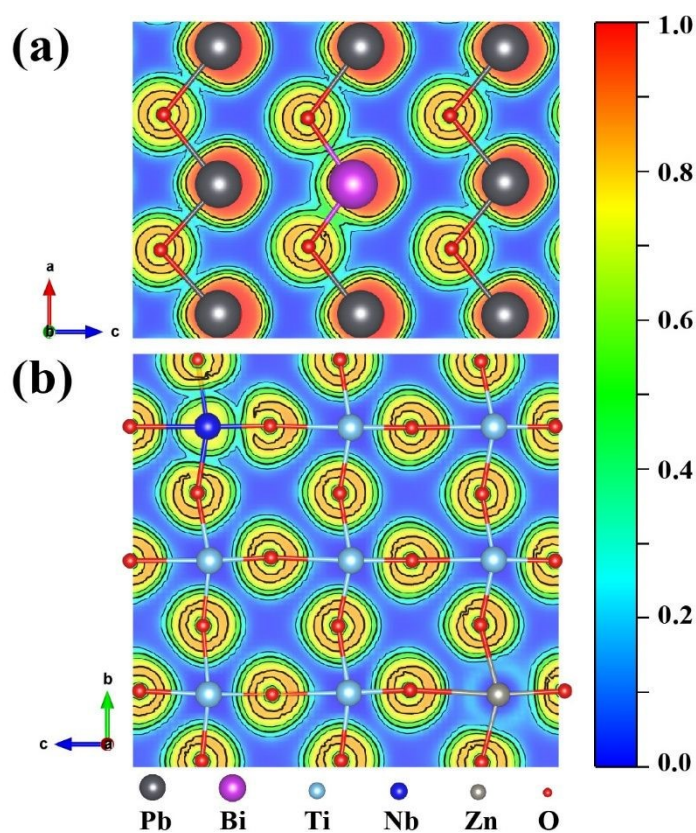
Fig. 5. Calculated electron localization function (ELF) and optimized crystal structure of 0.1BZN-0.9PT on (a) *ac* plane and (b) *bc* plane. The ELF values (0 to 1) are mapped on a blue-green-red color scale indicated on the right side.

To further understand the enhanced ferroelectric properties in the present 0.1BZN-0.9PT thin films, we conducted comprehensive ab-initio simulations. Since electric polarization arises from both ionic and electronic contributions, we first optimized the

crystal structure. The resulting atomic positions in the *A*-O and *B*-O planes are shown in Fig. 5. At the *B*-site, the average displacements of Ti, Nb, and Zn along the *z*-axis were found to be 0.20 Å, 0.26 Å, and 0.05 Å, respectively. These results indicate that the substitution of Nb for Ti at the *B*-site slightly enhances the electric polarization. At the *A*-site, Pb atoms remain largely centrosymmetric, with an average displacement of 0.07 Å. In contrast, the doped Bi atom exhibits a noticeable deviation, with a displacement of 0.18 Å, thereby contributing additional ionic polarization to the total electric polarization. To analyze the electronic contribution, we examined charge redistribution and asymmetric bonding interactions, which can be visualized using the electron localization function (ELF). Focusing on the *B*-site, we compared the bonding between Ti-O and Nb/Zn-O. Unlike the nearly pure ionic interaction between Ti and O (represented by the blue region in the ELF), the substituted Nb atom not only introduces more electrons into the system but also forms a more pronounced covalent bond with one of the nearest oxygen atoms, as shown in Fig. 5(b). This asymmetric charge redistribution provides the system with an additional degree of freedom for electric polarization, thereby enhancing the polarization value. Similarly, Zn substitution also contributes to the system's polarization, though the effect is much smaller and relatively insignificant compared to Nb, as illustrated by the cyan region around the Zn atom. At the *A*-site, the substitution of Bi results in an enlarged green area in the ELF, indicating increased electron sharing in the Bi-O bond and thus an enhanced covalent interaction.

Through Bader charge analysis, we can quantitatively elucidate the remarkable polarization enhancement resulting from Nb substitution. The calculated Bader charge

on the Ti atom is 1.92 e, exhibiting a deviation of 2.08 e from its ideal 4+ charge state. This deviation signifies the quantity of charge that does not contribute to ionic bond formation. Notably, the calculated Bader charge on Nb atoms is 2.68 e, which is 2.32 e lower than the ideal 5+ charge state. This pronounced deviation strongly suggests a significant decrease in the ionic character, thereby indicating a stronger covalent interaction between Nb and O atoms.

Conclusions

In summary, $0.1Bi(Zn_{2/3}Nb_{1/3})O_3$-$0.9PbTiO_3$ perovskite-type thin films were successfully fabricated via a conventional sol-gel method. Microstructural characterization reveals that the present thin films exhibit a homogeneous and dense morphology. Notably, the ferroelectric polarization properties are outstanding: the remanent polarization ($2P_r$) values measured by the normal mode and the PUND mode reach approximately 174 and 118 μC cm^{-2}, respectively. Moreover, the $0.1Bi(Zn_{2/3}Nb_{1/3})O_3$-$0.9PbTiO_3$ thin films possess a high Curie temperature (T_C) and a low leakage current. First-principles calculations demonstrate that the strong covalent interactions stemming from the hybridization of Pb/Bi-O and Ti/Zn/Nb-O bonds are responsible for the large ferroelectric polarization and elevated T_C. The excellent overall ferroelectric performance of the present thin films suggest that these films should be of interest for FeRAM applications.

See the supplementary material for Figures S1-3, including the HAADF image, temperature dependence of XRD patterns, and the leakage current density curves of the

0.1BZN-0.9PT thin films.

Author contributions

Mengqi Ye: Conceptualization, Data curation, Formal analysis, Methodology, Writing - original draft, Writing - review & editing. Jin Liu: Data curation, Formal analysis, Writing - original draft, Writing - review & editing. Duo Wang: Formal analysis, Methodology, Software, Writing - original draft, Writing - review & editing. Zhao Pan: Conceptualization, Data curation, Formal analysis, Funding acquisition, Investigation, Methodology, Project administration, Supervision, Writing - original draft, Writing - review & editing. Fengyi Zhou: Software, Writing - review & editing. Xubin Ye: Data curation. Huajie Luo: Data curation. Nianpeng Lu: Data curation, Writing - review & editing. Yunzhong Chen: Data curation, Writing - review & editing. Ruilong Wang: Supervisio, Writing - review & editing. Youwen Long: Funding acquisition, Supervision, Writing - review & editing.

Conflicts of interest

There are no conflicts of interest to declare.

Acknowledgements

References

1 I. Vrejoiu, M. Alexe, D. Hesse and U. Gösele, *Adv. Funct. Mater.*, 2008, **18**, 3892-3906.

2 J. F. Scott, *Science*, 2007, **315**, 954-959.

3 Y. L. Wang, H. Q. Zhao, L. X. Zhang, J. Chen and X. R. Xing, *Phys. Chem. Chem. Phys.*, 2017, **19**, 17493-17515.

4 H. Ruan, T. G. Saunders, H. Giddens, H. Zhang, A. A. Ihalage, J. F. Kolb, M. Blunt, S. Haq, H. Yan and Y. Hao, *J. Adv. Ceram.*, 2023, **12**, 1521-1532.

5 Y. Yan, Z. Li, J. Li, H. Du, M. Zhang, D. Zhang and Y. Hao, *ACS Appl. Mater. Interfaces*, 2021, **13**, 38517-38525.

6 G. Shirane, R. Pepinsky and B. C. Frazer, *Acta Cryst.*, 1956, **9**, 131-140.

7 R. E. Eitel, C. A. Randall, T. R. Shrout and S. E. Park, *Jpn J. Appl. Phys.*, 2002, **41**, 2099-2104.

8 T. Yoshimura and S. Trolier-McKinstry, *Appl. Phys. Lett.*, 2002, **81**, 2065-2066.

9 J. Xiao, A. Wu, P. M. Vilarinho, A. R. Ramos and E. Alves, *J. Mater. Chem.*, 2009, **19**, 5572-5579.

10 H. Wen, X. Wang, C. Zhong, L. Shu and L. Li, *Appl. Phys. Lett.*, 2007, **90**, 202902.

11 G. Wu, H. Zhou, X. Zhou, N. Qin and D. Bao, *J. Am. Ceram. Soc.*, 2010, **93**, 925-927.

12 S. Zhang, R. E. Eitel, C. A. Randall, T. R. Shrout and E. F. Alberta, *Appl. Phys. Lett.*, 2005, **86**, 262904.

13 G. A. Smolenskiĭ and I. E. Chupis, *Sov. Phys. Usp.*, 1982, **25**, 475-493.

14 J. Chen, K. Nittala, J. L. Jones, P. Hu and X. Xing, *Appl. Phys. Lett.*, 2010, **96**, 252908.

15 M. R. Suchomel, A. M. Fogg, M. Allix, H. Niu, J. B. Claridge and M. J. Rosseinsky, *Chem. Mater.*, 2006, **18**, 4987-4989.

16 A. A. Belik, *J. Solid. State. Chem.*, 2012, **195**, 32-40.

17 L. Zhang, J. Chen, H. Zhao, L. Fan, Y. Rong, J. Deng, R. Yu and X. Xing, *Dalton Trans.*, 2013, **42**, 585-590.

18 W. Song, G. Xi, Z. Pan, J. Liu, X. Ye, Z. Liu, X. Wang, P. Shan, L. Zhang, N. Lu, L. Fan, X. Qin and Y. Long, *Chin. Phys. B*, 2024, **33**, 057701.

19 Z. Xie, B. Peng, J. Zhang, X. Zhang, Z. Yue and L. Li, *J. Am. Ceram. Soc.*, 2015, **98**, 2968-2971.

20 J. Kim, T. Onaya, H. R. Park, Y. C. Jung, D.N. Le, M. Lee, H. Hernandez-Arriaga, Y. G. Zhang, E. H. R. Tsai, C. Nam, T. Nabatame, S. J. Kim, and J. Kim, *ACS Appl. Electron Mater.*, 2023, **5**, 4726-4745.

21 Y. Yun, P. Buragohain, M. Li, Z. Ahmadi, Y. Z. Zhang, X. Li, H. L. Wang, J. Li, P. Lu, L. L. Tao, H. Y. Wang, J. E. Shield, E. Y. Tsymbal, A. Gruverman, and X. S. Xu, *Nat. Mater.*, 2022, **21**, 903–909.

22 Y. L. Zhang, Q. X. Zhu, B. B. Tian, and C. G. Duan, *Nano-Micro Lett.*, 2024, **16**, 227.

23 H. M. Qin, N. He, C. Han, M. C. Zhang, Y. Wang, R. Hu, J. W. Wu, W. J. Shao, M Saadi, H Zhang, Y. D. Hu, Y. Liu, X. P. Wang, and Y. Tong, *Nanomaterials*, 2024, **14**(11), 986.

Physical Chemistry Chemical Physics Accepted Manuscript

24 R. Yu, H. Hojo, K. Oka, T. Watanuki, A. Machida, K. Shimizu, K. Nakano and M. Azuma, *Chem. Mater.*, 2015, **27**, 2012-2017

25 Z. Pan, J. Chen, L. Fan, Y. Rong, S. Zheng, L. Liu, L. Fang and X. Xing, *Mater. Res. Express*, 2014, **1**, 046301.

26 S. Chu, T. Chen, I. Tsai and W. Water, *Sensors and Actuators*, 2004, **113**, 198-203.

27 W. Gong, J. F. Li, X. Chu, Z. Gui and L. Li, *Acta Mater.*, 2004, **52**, 2787-2793.

28 C. Zhong, X. Wang, Y. Wu and L. Li, *J. Am. Ceram. Soc.*, 2010, **93**, 3993-3996.

29 C. Zhong, X. Wang, L. Guo and L. Li, *Thin Solid Films*, 2015, **580**, 52-55.

30 G. Kresse and J. Furthmüller, Phy. Rev. B, 1996, 54, 11169-11186.

31 J. P. Perdew, K. Burke and M. Ernzerhof, *Phy. Rev. Lett.*,1996, **77**, 3865-3868.

32 W. Kohn and L. J. Sham, *Phy. Rev.*, 1965, **140**, A1133-A1138.

33 A. Savin, R. Nesper, S. Wengert and T. F. Fässler, *Angew. Chem. Int. Ed.*, 1997, **36**, 1808-1832.

34 G. Henkelman, A. Arnaldsson and H. Jónsson. *Comp. Mater. Sci.*, 2006, **36**, 354-360.

35 E. K. Akdogan, C. J. Rawn, W. D. Porter and E. A. Payzant, *J. Appl. Phys.*, 2005, **97**, 084305.

36 B. Jiang, J. L. Peng, L. A. Bursill and W. L. Zhong, *J. Appl. Phys.*, 2000, **87**, 3462-3467.

37 T. Ohno, D. Suzuki, K. Ishikawa and H. Suzuki, *Adv. Powder Technol.*, 2007, **18**, 579-589.

38 N. J. Lóh, L. Simão, C. A. Faller, A. De Noni Jr and O.R.K. Montedo, *Ceram. Int.*, 2016, **42**, 12556-12572.

39 K. R. Kambale, A. Mahajan and S. P. Butee, *Metal Powder Report*, 2021, **74**, 130-136.

40 S. Martin, N. Baboux, D. Albertini and B. Gautier, *Ultramicroscopy*, 2017, **172**, 47-51.

41 S. Martin, N. Baboux, D. Albertini and B. Gautier, *Rev. Sci. Instrum.*, 2017, **88**, 023901.

42 X. W. Jiang, Q. Yang, and J. X. Ca, *Phy. Lett. A*, 2016, **380**, 1071-1074.

43 J. F. Scott, L. Kammerdiner, M. Parris, S. Traynor, V. Ottenbacher, A. Shawabkeh and W. F. Oliver, *J. Appl. Phys.*, 1988, **64**, 787-792.

44 X. Shi, Y. Chen, W. Shi and L. Wang , *Seventh International Conference on Thin Film Physics and Applications*, 2011, Proceedings **Vol. 7995**, 79951N.

45 S. Yasuoka, R. Mizutani, R. Ota, T.a Shiraishi, T. Shimizu, S. Yasui, Y. Ehara, K. Nishida, M. Uehara, H. Yamada, M. Akiyama, Y. Imai, O. Sakata and H. Funakubo, *J. Ceram. Soc. Jpn.*, 2022, **130**, 436-441.

46 Y. Zhang, Q. Zhu, B. Tian and C. Duan, *Nano-Micro Lett.*, 2024, **16**, 227.

47 T. Leist, T. Granzow, W. Jo and J. Rödel, *J. Appl. Phys.*, 2010, **108**, 014103.

48 Y. H. Shin, I. Grinberg, I. W.Chen and M. R. Andrew, *Nature*, 2007, **449**, 881-884.

49 Z. Pan, J. Chen, L. Fan, H. Liu, L. Zhang, L. Hu, Y. Ren, L. Liu, L. Fang, X. A. Fan, Y. W. Li and X. R. Xing, *Inorg. Chem. Front.*, 2017, **4**, 1352-1355.

50 Z. Pan, J. Chen, R. Yu, L. Patra, P. Ravindran, A. Sanson, R. Milazzo, A. Carnera, L. Hu, L. Wang, H. Yamamoto, Y. Ren, Q. Z. Huang, Y. Sakai, T. Nishikubo, T. Ogata, X. A. Fan, Y. W. Li, G. Q. Li, H. Hojo, M. Azuma and X. R. Xing, *Chem. Mater.*, 2019, **31**, 1296-1303.

51 L. J. Liu, S. K. Ren, J. Zhang, B. L. Peng, L. Fang and D.W. Wang, *J. Am. Ceram. Soc.*, 2018,

101, 2408-2416.

52 S. Dolabella, A. Borzì, A. Dommann and A. Neels, *Small Methods*, 2022, **6**, 2100932.

53 Z. J. Jiang, B. Xu, S. Prosandeev, Y. Nahas, S. Prokhorenko, J. Íñiguez and L. Bellaiche, *Phys. Rev. B*, 2021, **103**, L100102.

54 X. R. Wang, H. F. Guo, C. Zhou and J. K. Bai, *BioMed. Eng. OnLine*, 2021, **20**, 86.

Physical Chemistry Chemical Physics Accepted Manuscript

All the data have been included in the article.